Optics Letters

High-quality partially coherent Bessel beam array generation

Chunhao Liang,[1,3] Xinlei Zhu,[1] Chenkun Mi,[1] Xiaofeng Peng,[1] Fei Wang,[1,4] Yangjian Cai,[1,2,5] and Sergey A. Ponomarenko[3,*]

[1]College of Physics, Optoelectrics and Energy & Collaborative Innovation Center of Suzhou Nano Science and Technology, Soochow University, Suzhou 215006, China
[2]Center of Light Manipulations and Applications, College of Physics and Electronics, Shandong Normal University, Jinan 250014, China
[3]Department of Electrical and Computer Engineering, Dalhousie University, Halifax, Nova Scotia B3J2X4, Canada
[4]e-mail: fwang@suda.edu.cn
[5]e-mail: yangjiancai@suda.edu.cn
*Corresponding author: serpo@dal.ca

Received 15 May 2018; accepted 5 June 2018; posted 7 June 2018 (Doc. ID 331753); published 29 June 2018

We propose a protocol for generating high-quality, partially coherent (quasi-)Bessel beam arrays with controllable beam order and spatial distributions. Our protocol involves, apart from beam intensity shaping, coherence engineering of recently introduced optical coherence lattices. Our theoretical results are validated with the experimental realization of partially coherent Bessel beam arrays. The novel beam arrays are anticipated to be useful for multi-particle trapping and micromanipulation, optical metrology and microscopy, as well as for 3D imaging.

OCIS codes: (030.0030) Coherence and statistical optics; (030.1670) Coherent optical effects; (140.3290) Laser arrays; (140.3300) Laser beam shaping.

https://doi.org/10.1364/OL.43.003188

Diffraction is a ubiquitous phenomenon in physical optics, affecting any optical wave packet of a finite spatial extent. It was shown by Durnin [1], however, that Bessel beams, containing a central lobe surrounded by a series of concentric rings, display remarkable resilience to diffraction over long propagation distances. In addition, Bessel beams exhibit a self-healing property when scattered from fine scale obstacles [2]. These features make Bessel beams especially attractive for particle trapping, atomic guiding, optical micromanipulation, microscopy, and cell imaging, to mention but a few applications [3–6]. Realistic Bessel beams cannot of course carry infinite power, and hence they have to be apertured; we are concerned with such (quasi-) Bessel beams hereafter.

Further, periodic beam arrays have crucial applications to cold atom trapping, optical grating design, microfluidic sorting, photonic crystals engineering, and optical communications [7–12]. There has been reported a multitude of methods to generate coherent and partially coherent beam arrays to date [9,13–19]. In this context, (quasi-)Bessel beam arrays (BBAs), can find widespread applications to real-time volumetric imaging, transverse blood flow velocimetry [10], microparticle guiding [11], and spatiotemporal soliton stabilization [12], for example. There have been a considerable number of methods reported for BBA generation so far [15–19]. However, the existing approaches suffer from considerable shortcomings such as low beam quality [15–18], poor beam order control [15,19], and reliance on rather uncommon optical materials [19].

As is well known, an annular aperture can be used to generate a Bessel beam [20]. It has been recently shown theoretically [21] and demonstrated experimentally [22] that optical coherence lattices (OCLs) can be used to generate beam arrays. In this Letter, we combine the functionality of the annular aperture and the OCLs to generate partially coherent BBAs of highly controllable beam orders and spatial distributions via spatial coherence periodicity engineering.

As a starting point, we recall that second-order statistical properties of scalar optical fields can be characterized by the cross-spectral density in the space-frequency domain. In particular, the genuine cross-spectral density of a Schell-model-type partially coherent beam can be represented as [23]

$$W^{(0)}(\boldsymbol{\rho}_1,\boldsymbol{\rho}_2) = \tau^*(\boldsymbol{\rho}_1)\tau(\boldsymbol{\rho}_2)\mu(\boldsymbol{\rho}_2-\boldsymbol{\rho}_1) = \tau^*(\boldsymbol{\rho}_1)\tau(\boldsymbol{\rho}_2)\tilde{p}(\boldsymbol{\rho}_2-\boldsymbol{\rho}_1), \quad (1)$$

where $\boldsymbol{\rho}_i (i = 1, 2)$ is a position vector in the source plane, $\tau(\boldsymbol{\rho})$ an arbitrary complex function, and $\tilde{p}$ a Fourier transform of a non-negative function p. If a Schell-model source is generated by spatially modulating—for instance, via a finite aperture of an imaging system—a statistically homogeneous source with the spectral degree of coherence μ, $\tau(\boldsymbol{\rho})$ can represent an aperture function of the imaging system. We will assume it to be the case hereafter.

Further, we assume, following [21], that the p function is given by

$$p(\mathbf{v}) = \frac{1}{M}\sum_{n=1}^{M}\delta(\mathbf{v}-\mathbf{V}_{0n}), \quad (2)$$

where $\mathbf{V}_{0n} = (V_{0xn}, V_{0yn})$ is an off-axis displacement, and δ is a Dirac delta function. Using Eq. (2), we can rewrite the source degree of coherence as

$$\mu(\boldsymbol{\rho}_2 - \boldsymbol{\rho}_1) = \frac{1}{M}\sum_{n=1}^{M} \exp[-i(\boldsymbol{\rho}_2 - \boldsymbol{\rho}_1)\cdot \mathbf{V}_{0n}]. \tag{3}$$

Eq. (3) specifies the degree of coherence of an OCL; this class of partially coherent beams was theoretically introduced in Ref. [21], and OCLs were experimentally realized in Ref. [22].

Next, the radiant intensity of any paraxial, partially coherent field can be shown to be related to the cross-spectral density at the source as [24]

$$I(\mathbf{s}) \propto \tilde{W}^{(0)}(-k\mathbf{s}_\perp, k\mathbf{s}_\perp), \tag{4}$$

where the tilde represents a Fourier transform; $\mathbf{s}_\perp$ is a 2D projection onto the source plane of the unit vector $\mathbf{s}$ pointing from the origin to a far-field observation point, and $k = 2\pi/\lambda$ with λ being the wavelength of light.

It follows at once from Eqs. (1) and (4) that the radiant intensity can be expressed as [25]

$$I(\mathbf{s}) \propto |\tilde{\tau}(-k\mathbf{s}_\perp)|^2 \otimes p(-k\mathbf{s}_\perp), \tag{5}$$

where "$\otimes$" denotes a convolution. In this expression, p plays the role of a sampling function for the complex valued aperture profile function $\tilde{\tau}$. In case of sampling with an ideal OCL, given by Eq. (2), Eq. (5), takes the form

$$I(\mathbf{s}) \propto \sum_{n=1}^{M} \left|\tilde{\tau}[k(\mathbf{s}_\perp + \mathbf{V}_{0n})]\right|^2. \tag{6}$$

To generate an ideal BBA, we choose τ as

$$\tau(\rho, \theta) = \delta(\rho - R)\exp(il\theta), \tag{7}$$

where (ρ, θ) are polar coordinates. Eq. (7) describes a combined action of an infinitely thin annular aperture of radius R and a spiral phase plate imposing a topological charge l on a transmitted beam.

On substituting Eq. (7) into Eq. (6), we obtain the radiant intensity of an ideal BBA in the form

$$I(\mathbf{s}) \propto \sum_{n=1}^{M} J_l^2(kR|\mathbf{s}_\perp + \mathbf{V}_{0n}|). \tag{8}$$

Eq. (8) clearly represents an array of uncorrelated ideal Bessel beams, each component having the same topological charge l.

To touch base with the laboratory realization of the proposed partially coherent BBAs, we consider an OCL with a finite node width w_s, modeled by a Gaussian array as

$$p(\mathbf{v}) = \frac{1}{M}\sum_{n=1}^{M} \exp[-(\mathbf{v} - \mathbf{V}_{0n})^2/2w_s^2]. \tag{9}$$

Here, w_s should be much smaller than the width of $\tilde{\tau}$ to ensure efficient sampling. Further, we approximate the ideal complex aperture function of Eq. (7) viz.,

$$\tau(\rho, \theta) = [\mathrm{circ}(\rho/a) - \mathrm{circ}(\rho/b)]\exp(il\theta), \tag{10}$$

where the constraint $a > b \gg a - b$ is imposed on the magnitudes of the inner and outer radii b and a, of the annual aperture, respectively. Further, circ is a circular function. We will refer to these non-ideal BBAs, simulated numerically and generated experimentally, as quasi-BBAs. In the experiment, the generation of high-quality partially coherent quasi-BBAs is ensured by minimizing the ratio $(a - b)/b$.

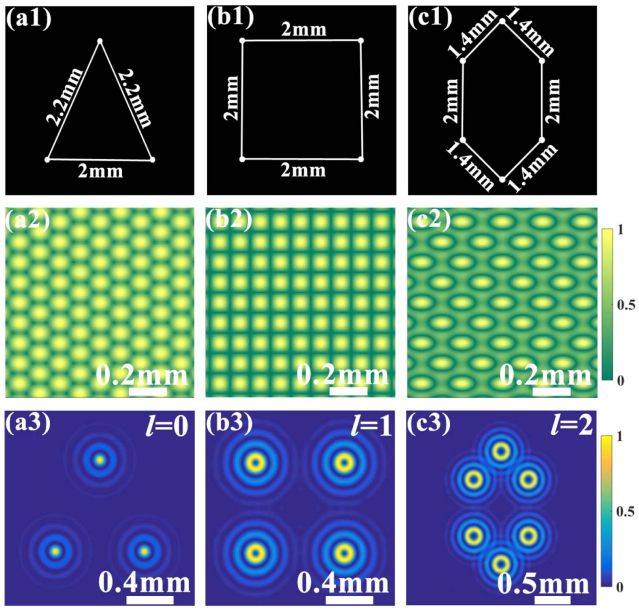

Fig. 1. (a1)–(c1) OCL distributions p with triangular, square, and hexagonal patterns, respectively; (a2)–(c2) modulus of the source degree of coherence $|\mu|$ of the corresponding OCLs; (a3)–(c3) radiant intensity distributions of the generated quasi-BBAs with different beam orders. The radiant intensity distributions are normalized by the peak intensity.

In Fig. 1, we display the sampling function p (first row), the magnitude of the degree of coherence (second row), and the radiant intensity (third row) distributions of numerically simulated quasi-BBAs for triangular, square, and hexagonal OCLs. The results are obtained with the fast Fourier transform (FFT) algorithm in MATLAB using Eqs. (1)–(3), (6), and (10). In our simulations, we choose the aperture function parameters as $a = 0.5$ m, $b = 0.35$ m. The geometrical structure of the function p is shown in Figs. 1(a1)–1(c1). Our results in Figs. 1(a3)–1(c3) prove the theoretical possibility of quasi-BBAs generation with highly controllable beam orders and spatial distributions.

We now describe the experimental generation of partially coherent quasi-BBAs. The experimental setup is illustrated in Fig. 2. A laser beam, emitted from Nd:YAG, is expanded

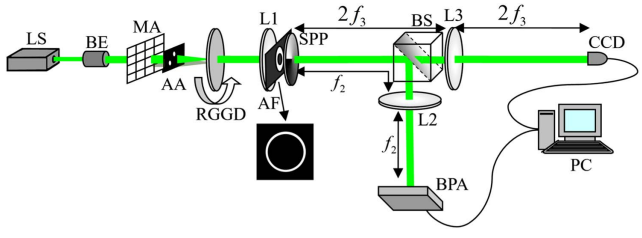

Fig. 2. Experimental setup for generation and measurement of different beam order quasi-BBAs; laser, Nd:YAG laser; BE, beam expander; MA, microlens array; AA, amplitude aperture; RGGD, rotating ground-glass disk; L1, L2, and L3, thin lenses; SPP, spiral phase plate; AF, amplitude filter; BS, beam splitter; CCD, charge-coupled device; BPA, beam profile analyzer; PC, personal computer.

by a beam expander (BE) to convert it to effectively a plane wave—to a beam with the Rayleigh range far exceeding the laboratory size to be precise—such that the intensity in a small central area of the beam can be considered uniformly spatially distributed. The central spot is then focused by a microlens array (MA) with the focal length $f = 65.6$ mm $\pm$ 3%. MA is comprised of nine microlenses, the dimensions of each microlens being 1 × 1 mm. An amplitude aperture (AA), placed between the MA and the rotating ground-glass disk (RGGD), is used to control the spatial distribution of sampling points. The AA is comprised of several holes with a diameter of about 1.0 mm each. In the experiment, we use triangular, square, or hexagonal patterned AAs to generate the corresponding quasi-BBAs, as shown in Figs. 1(a3)–1(c3). The transmitted beam spot from the AA is focused on the RGGD, which is located in the back focal plane of the MA. Hence, the beam transmitted through RGGD, made up of a number of fine speckles, serves as a (sampling) function p. As a precise spatial intensity distribution across each speckle is irrelevant, we approximate the intensity distribution across the speckle with a Gaussian. The intensity pattern after the RGGD can be evaluated by a beam profile analyzer (BPA), and through a numerical fit to the experimental results, we obtain for the spot size of each Gaussian beam $w_s = 21.2$ μm. The light emerging from the RGGD is collimated by a thin lens L1 with focal length $f_1 = 400$ mm to form an OCL. The generated OCL is then modulated by an annular aperture, shown in the inset of Fig. 2 and by a spiral phase plate (SPP), which are used in concert to generate a quasi-Bessel beam and control its topological charge. The annular aperture in Fig. 2 is labeled as an amplitude filter (AF); its parameters are $a = 0.5$ mm and $b = 0.35$ mm. This procedure realizes the complex AA function of Eq. (10) in the laboratory.

Next, the aperture modulated OCL is split by a beam splitter (BS), and the transmitted beam, after passing through a thin lens L3 with focal length $f_3 = 150$ mm, arrives at a charge-coupled device (CCD). The distances from L3 to AF and from L3 to CCD are $2f_3$, which indicates the degree of coherence in the plane of CCD is the same as that in the source plane (just behind AF). The instantaneous intensity recorded by CCD can be used to recover the source degree of coherence from the normalized fourth-order correlation function, assuming Gaussian statistics of the source [26]. We obtain the source coherence width $\delta_0 = 3.2$ mm through a numerical fit to the experimental results.

Further, the reflected beam that is focused by a thin lens L2 with focal length $f_2 = 150$ mm then arrives at BPA. Both distances, from L2 to AF and from L2 to BPA, are equal to f_2. This procedure allows us to obtain far-field intensity distributions of quasi-BBAs with different topological charges controlled by SPP.

We now compare our experimental results with our simulations. To faithfully reproduce the experimental conditions, we will make use of the acquired experimental data for all the corresponding simulation parameters. To make connection with the experimental situation we define a Fourier transform in Eq. (5) as

$$\tilde{\tau}(\mathbf{s}_\perp) \propto \int \tau(\boldsymbol{\rho}) \exp(-ik\mathbf{s}_\perp \cdot \boldsymbol{\rho}/f_2)\mathrm{d}^2\rho. \tag{11}$$

In Figs. 3(a)–3(c), we present the density plots of experimentally generated triangular, square, and hexagonal patterned

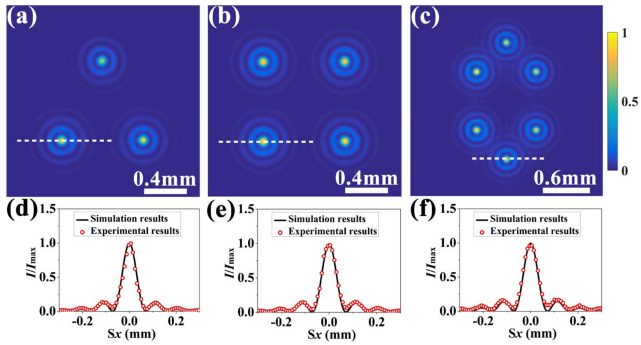

Fig. 3. (a)–(c) Experimental results for far-field normalized intensity distributions of OCLs, modulated by an annular aperture with no spiral phase plate inserted—corresponding to BBAs with $l = 0$. (d)–(f) One-dimensional intensity distributions of individual Bessel beamlets, marked by white dashed lines in (a)–(c), across the dashed lines, obtained experimentally (red dots), and in simulations (solid lines).

partially coherent quasi-BBAs. In this experiment, the OCLs are shaped by the annular aperture alone (no SPP inserted anywhere). Thus, the individual beamlets in a BBA are vortex free. As one can see in Figs. 3(a)–3(c), the array background is free of any speckle noise. To examine the individual Bessel beamlet quality in an array, we plot in Figs. 3(d)–3(f) the normalized one-dimensional (1D) intensity distributions corresponding to the beamlets marked with white dashed lines in Figs. 3(a)–3(c). The corresponding theoretical results are also shown in Figs. 3(d)–3(f) for comparison. In our simulations, we considered ideal OCLs with infinitely small node widths and found our experimental results in excellent agreement with the simulations, as evidenced by Figs. 3(d)–3(f).

To demonstrate efficient control of the BBA topological charge in our protocol, SPPs with topological charges $l = 1$ or 2 were inserted behind the AF. In this procedure, SPPs should be carefully aligned to ensure that the phase singularity lies on the AF symmetry axis.

In Figs. 4(a) and 4(b), we display our experimental results for the normalized intensity distributions of square BBAs with $l = 1$ and 2. The 1D intensity distributions of individual beamlets and the corresponding theoretical results are exhibited

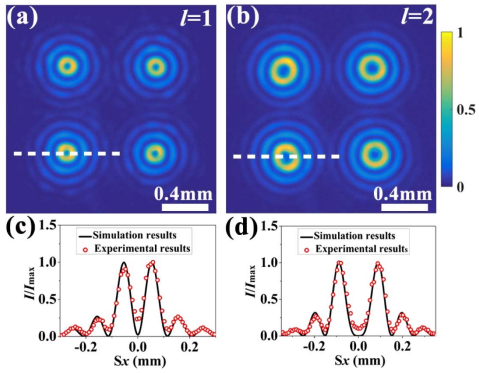

Fig. 4. (a) and (b) Experimental results for the normalized intensity distributions of partially coherent BBAs with topological charges $l = 1$ and 2. (c) and (d) One-dimensional intensity distributions of individual Bessel beamlets, marked by white dashed lines in (a) and (b), across the dashed lines, obtained experimentally (red dots), and in simulations (solid lines).

in Figs. 4(c) and 4(d). We observe that the individual beamlet concentric rings in Figs. 4(a) and 4(b) are rougher on the edges than are those of the vortex-free BBA beamlets. This is likely because there is a slight deviation of the vortex phase imparted by the SPP on a beamlet in the experiment from an ideal vortex phase in theory due to the imperfections introduced by an SPP manufacturing process. Next, we can infer from Figs. 4(c) and 4(d) that the beamlet intensity at a dark vortex core does not vanish. This is a common feature of partially coherent vortex beams. It is a consequence of the fact that unless such beams are judicially engineered to maintain their vortex structure on free-space propagation [27,28], the imperfect correlation of plane waves, comprising the beam angular spectrum and leading to a perfect source intensity null at the vortex core, results in gradual "filling" of the core upon vortex beam propagation in free space [29].

Further, we note that the energy utilization in our experiment is about 5%. Most of the energy is lost due to source light scattering by the RGGD and AF (annular aperture). This poses no problem as long as no high intensity is required for a particular application. To reduce energy losses, one may also use an optical-axicon-based method of generating individual Bessel beams [30]. Finally, the generated beam arrays are not sensitive to the RGGD alignment. Yet, the BBA quality is affected by the AF geometrical parameters, since the OCL node width cannot be made arbitrarily small in the experiment.

In summary, we proposed a protocol to generate high-quality, partially coherent BBAs with highly controllable beam orders and spatial distributions. We numerically simulated the generation of partially coherent non-ideal quasi-BBAs. We verified our protocol by experimentally realizing the advanced quasi-BBAs and found our simulations in reasonable agreement with our experimental results. The proposed BBAs are expected to find applications to multi-particle trapping and micromanipulation, optical metrology and microscopy, as well as to 3D imaging.

Funding. Natural Sciences and Engineering Research Council of Canada (NSERC); National Natural Science Foundation of China (NSFC).

REFERENCES

1. J. Durnin, J. Opt. Soc. Am. A **4**, 651 (1987).
2. Z. Bouchal, J. Wagner, and M. Chlup, Opt. Commun. **151**, 207 (1998).
3. D. G. Grier, Nature **424**, 810 (2003).
4. F. O. Fahrbach, P. Simon, and A. Rohrbach, Nat. Photonics. **4**, 780 (2010).
5. T. A. Planchon, L. Gao, D. E. Milkie, M. W. Davidson, J. A. Galbraith, C. G. Galbraith, and E. Betzig, Nat. Methods **8**, 417 (2011).
6. J. Chen, J. Ng, Z. Lin, and C. T. Chan, Nat. Photonics **5**, 531 (2011).
7. X. Liu, J. Yu, Y. Cai, and S. A. Ponomarenko, Opt. Lett. **41**, 4182 (2016).
8. M. MacDonald, G. Spalding, and K. Dholakia, Nature **426**, 421 (2003).
9. L. Ma and S. A. Ponomarenko, Opt. Express **23**, 1848 (2015).
10. J. Lu, Int. J. Imaging Syst. Technol. **8**, 126 (1997).
11. B. P. S. Ahluwalia, X. C. Yuan, S. H. Tao, J. Bu, H. Wang, X. Peng, and H. B. Niu, Appl. Phys. Lett. **87**, 084104 (2005).
12. D. Mihalache, D. Mazilu, F. Lederer, B. A. Malomed, Y. V. Kartashov, L. C. Crasovan, and L. Torner, Phys. Rev. Lett. **95**, 023902 (2005).
13. R. K. Singh, A. M. Sharma, and P. Senthilkumaran, Opt. Lett. **40**, 2751 (2015).
14. C. Liang, C. Mi, F. Wang, C. Zhao, Y. Cai, and S. A. Ponomarenko, Opt. Express **25**, 9872 (2017).
15. N. Guerineu and J. Primot, J. Opt. Soc. Am. A **16**, 293 (1999).
16. Z. Bouchal, Opt. Lett. **27**, 1376 (2002).
17. E. Stankevičius, M. Garliauskas, M. Gedvilas, and G. Račiukaitis, Opt. Express **23**, 28557 (2015).
18. Y. Lu, B. Jiang, S. Lü, Y. Liu, S. Li, Z. Cao, and X. Qi, Opt. Commun. **363**, 85 (2016).
19. S. H. Tao, X. C. Yuan, and B. S. Ahluwalia, J. Opt. A **7**, 40 (2005).
20. J. Durnin, J. Miceli, and J. H. Eberly, Phys. Rev. Lett. **58**, 1499 (1987).
21. L. Ma and S. A. Ponomarenko, Opt. Lett. **39**, 6656 (2014).
22. Y. Chen, S. A. Ponomarenko, and Y. Cai, Appl. Phys. Lett. **109**, 061107 (2016).
23. F. Gori and M. Santarsiero, Opt. Lett. **32**, 3531 (2007).
24. L. Mandel and E. Wolf, *Optical Coherence and Quantum Optics* (Cambridge University, 1995).
25. F. Wang and O. Korotkova, Opt. Lett. **41**, 1546 (2016).
26. C. Liang, F. Wang, X. Liu, Y. Cai, and O. Korotkova, Opt. Lett. **39**, 769 (2014).
27. S. A. Ponomarenko, J. Opt. Soc. Am. A **18**, 150 (2001).
28. G. V. Bogatyryova, C. V. Felde, P. Polyanskii, S. A. Ponomarenko, M. S. Soskin, and E. Wolf, Opt. Lett. **28**, 878 (2003).
29. Y. Yang, M. Mazilu, and K. Dholakia, Opt. Lett. **37**, 4949 (2012).
30. S. V. Popov and A. T. Friberg, Opt. Eng. **34**, 2567 (1995).